Dark Matter Gravitational Clustering With a Long-Range Scalar Interaction

Wojciech A. Hellwing[1,*] and Roman Juszkiewicz[1,2,†]

[1] *Nicolaus Copernicus Astronomical Center, Bartycka 18, 00-719 Warsaw, Poland*
[2] *Institute of Astronomy, University of Zielona Góra, ul. Lubuska 2, Zielona Góra, Poland*

(Dated: 11 September 2008)

We explore the possibility to improve the ΛCDM model at megaparsec scales by introducing a scalar interaction which increases the mutual gravitational attraction of dark matter particles. Using N-body simulations, we study the spatial distribution of dark matter particles and halos. We measure the effect of modifications in the Newton's gravity on properties of the two-point correlation function, the dark matter power spectrum and the cumulative halo mass function. The results look promising: the scalar interaction improves the agreement between theoretical predictions and observations at megaparsec scales without spoiling the ΛCDM successes at larger scales.

PACS numbers: 98.80.-k, 11.25.-w, 95.35.+d, 98.65.Dx

arXiv:0809.1976v2 [astro-ph] 13 Sep 2008

I. INTRODUCTION

The ΛCDM model successfully passes almost all observational tests (see WAMP recent results [1]). It does, however, experience some difficulties. They appear at length scales below few megaparsecs. The model is less effective in evacuating cosmic voids than the real Universe. It also shows high accretion rate of intergalactic debris onto galaxies continuing to the present time, contrary to observational evidence. The very existence of large galaxies like our Milky Way, with its spiral structure intact, and suggesting lack of mergers in recent history appears to be inconsistent with the ΛCDM simulations. For an excellent discussion of the observational situation and comparison with the ΛCDM model, see Refs. [2], [3] and [4], and the references therein.

To improve the agreement of the standard model with the observations at small scales without spoiling the successes at large scales, G. Farrar and J. Peebles [5] have recently proposed a modification of the gravitational force acting between two dark matter (DM) particles (see also Refs.). The physical motivation for this model comes from the string theory (cf. Ref. [6] on string gas cosmology theory). These theoretical suggestions were followed by the work of Nusser et al. [3], exploring the cosmological implications with N-body simulations. Some perliminary results on similiar scalar model was also obtained by Rodríguez-Meza et al. [7, 8, 9]. Our own work, presented here should be regarded as the next step in this line of research. Like Nusser et al., we study the two-point correlation function and the statistical properties of the mass distribution of the dark matter halos. To our knowledge, for the first time in the literature, we also study the power spectra for a set of scalar field parameters. Although the number of particles in our simulations is the same as in those used by Nusser et al. and our resolution is similar to their resolution, we consider a wider range of scalar model parameters. As a consequence, we do resolve the power spectrum near the screening length characteristic scale. Our results show a clear feature in the power spectrum near a wavenumber, which is the inverse of the screening length. The extra power seen at higher wavenumbers is generated by the gravitational field, enhanced by the scalar interaction. Nusser et al. could not see a similar feature in their correlation function because the screening lengths they considered were too close to the mean interparticle separation in their simulations. Apart from this important difference, we confirm their results. The scalar field generates lower density in voids. It also suppresses low redshift accretion.

This paper is organized as follows: In section II we present the effective gravitational potential we use as an approximation of the scalar field. In section III we describe our N-body simulations. Our results are presented in Section IV. A brief summary and discussion appears in section V.

II. THEORY

Following Refs. [10, 11], we consider DM particles as strings. Their dynamics is defined by conventional gravity as well as an additional attractive force, induced by an exchange of a massless scalar. This force is well represented by a Yukawa-like potential with a characteristic screening length dynamically generated by the presence of the light particles coupled to scalar (see Ref. [5] for details on dynamical screening mechanism). We consider one species of strings as DM particles. The force between two DM particles, each of mass m, arises from the potential

$$\Phi(\mathbf{r}) = -\frac{Gm}{r}\, g(x)\ , \tag{1}$$

with

$$g(x) \;=\; 1 + \beta\, e^{-x/r_s}\,. \tag{2}$$

*Electronic address: pchela@camk.edu.pl
†Electronic address: roman@camk.edu.pl

Here G is Newton's constant; $\mathbf{r}$ and $\mathbf{x} = \mathbf{r}/a(t)$ are, respectively, the particle separation vector in real space and comoving coordinates; t is the cosmological time; a is the scale factor, normalized to unity at present,

$$a(t_0) \;=\; 1\,. \tag{3}$$

Here and below the subscript "0" denotes the present epoch. The parameter r_s is the screening length and β is a measure of the relative strength of the scalar interaction compared to conventional gravity. The screening length r_s is constant in comoving coordinates because of the dynamical screening mechanism, specific to the class of scalar fields considered here [10, 11].

Switching from the discrete particle picture to fluid dynamics, we will now introduce the dark matter density field, given by the expression

$$\rho(\mathbf{x}, t) = \langle\rho\rangle\;(1+\delta)\,, \tag{4}$$

where $\langle\rho(t)\rangle$ is the ensemble average of the dark matter density at time t, and $\delta(\mathbf{x}, t)$ describes local deviations from homogeneity. The structure formation is driven only by the spatially fluctuating part of the gravitational potential, $\phi(\mathbf{x}, t)$, induced by the density fluctuation field δ,

$$\frac{\phi(\mathbf{x})}{G\langle\rho\rangle a^2} \;=\; -\int \frac{d^3\mathbf{x}'\delta(\mathbf{x}')}{|\mathbf{x}-\mathbf{x}'|} g\left(|\mathbf{x}-\mathbf{x}'|\right)\,. \tag{5}$$

The Fourier transform of this equation is

$$\phi_{\mathbf{k}} = -\frac{3H_0^2\Omega_M}{2a}\,\frac{\delta_{\mathbf{k}}}{k^2}\left[1+\frac{\beta}{1+(kr_s)^{-2}}\right]\,, \tag{6}$$

where

$$\phi_{\mathbf{k}} \;\equiv\; (2\pi)^{-2/3}\int \phi(\mathbf{x})\,e^{-i\mathbf{k}\cdot\mathbf{x}}\,d^3\mathbf{x} \tag{7}$$

and

$$\delta_{\mathbf{k}} \;\equiv\; (2\pi)^{-2/3}\int \delta(\mathbf{x})\,e^{-i\mathbf{k}\cdot\mathbf{x}}\,d^3\mathbf{x} \tag{8}$$

are the Fourier transforms of $\phi(\mathbf{x})$, and $\delta(\mathbf{x})$, respectively; $\mathbf{k}$ is the comoving wavevector, and the quantities

$$\Omega_M \;\equiv\; 8\pi G\,\langle\rho\rangle_0\;/3H_0^2 \tag{9}$$

and H_0 are, respectively, the present values of the dimesionless mean dark matter density and the Hubble parameter. From now on, we will also use the symbols h and Ω_Λ, denoting the dimensionless H_0, expressed in units of 100 km s^{-1}Mpc^{-1}, and the cosmological constant contribution to the present mean density.

Note that when $\beta = 0$ or $x \gg r_s$, equations (5) and (6) become identical with conventional gravity [12]. Indeed, consider the fractional deviation from the Newtonian gravitational potential,

$$\frac{\Delta\phi_{\mathbf{k}}}{\phi_{\mathbf{k}}} \;\equiv\; \frac{\phi_{\mathbf{k}}-\phi_{\mathbf{k}}^{\rm N}}{\phi_{\mathbf{k}}^{\rm N}}\,. \tag{10}$$

Throughout this paper, the label 'Newton', and the subscript 'N' refer to the ΛCDM cosmology with the conventional Newtonian gravity. Equation (6) gives

$$\frac{\Delta\phi_{\mathbf{k}}}{\phi_{\mathbf{k}}} \;=\; \frac{\beta}{1+(kr_s)^{-2}}\quad. \tag{11}$$

This is the Fourier image of the spatial decline of the Yukawa potential: in the limit $kr_s \to 0$, the above expression vanishes. In the opposite limit, the fractional deviation from Newtonian gravity reaches a finite value,

$$\Delta\phi_{\mathbf{k}}/\phi_{\mathbf{k}} \to \beta \quad \text{for}\;\; kr_s \gg 1, \tag{12}$$

$$\Delta\phi_{\mathbf{k}}/\phi_{\mathbf{k}} \to 0 \quad \text{for}\;\; kr_s \ll 1\,. \tag{13}$$

We consider values of β of order unity and screening lengths of order of few megaparsecs or smaller. Therefore, we can expect that our model predictions differ from the ΛCDM cosmology only on scales $\sim 1h^{-1}$ Mpc, while on larger scales these two models are indistinguishable, unlike other modifications of gravity, considered recently, for example the DGP model [13], $f(R)$ theories [14] ,modifications of the Newtionan gravity on megaparsec scales [15, 16, 17, 18] or MONDian cosmological simulations [19].

Here we study only the distribution of the dynamically dominant dark matter particles. We will study the baryon distribution as well in our next paper.

III. SIMULATIONS

In this section we describe our numerical experiments.

A. Initial Conditions

To set up the initial conditions, we have to define the power spectrum of the dark matter density fluctuations,

$$P(k) \;=\; \left\langle|\delta_{\mathbf{k}}|^2\right\rangle\,. \tag{14}$$

We use a power spectrum, derived from the `cmbfast` code by Seljak & Zaldarriaga [20] with cosmological parameters $h = 0.7$, $\Omega_M = 0.3$, $\Omega_\Lambda = 0.7$ and $\sigma_8 = 0.8$. The last in this set of parameters is the present value of the root-mean-square density contrast of dark matter spatial fluctuations within a 8 h^{-1} Mpc sphere. This is the conventional normalization parameter and a measure of the degree of inhomogeneity of the dark matter distribution.

The resulting power spectrum, together with the `PMcode` by Klypin & Holtzman [21] is used to displace 128^3 particles from their regular lattice positions, following the Zel'dovich approximation (see Ref. [22] for details). The number of individual simulations for each set of model parameters has to be large enough to allow a decent average over simulation-to-simulation phase fluctuations. We decided that for our purposes "a large enough number" = 5 to 10, depending on the size of the simulation box.

B. The code

We use the open source code AMIGA (*Adaptive Mesh Investigations of Galaxy Assembly*) by Knebe, Green, Gill & Saar which is the successor of the MLAPM code [23]. AMIGA is a *Particle Mesh* code with implementation of *the Adaptive Mesh Refinements*(AMR) technique to obtain high force resolution. We have turned off the AMR part of the code leaving only the pure PM kernel, reducing the simulation time at the expense of the force resolution. To accommodate for the poor force resolution we have divided our simulations into two sets.

The first set of simulations was used to study the power spectrum and the spatial correlation function of the dark matter density fluctuations. The simulation box in this series of simulations has a width $200h^{-1}$ Mpc, allowing a proper treatment of the fundamental mode of density perturbations, which remains in the linear regime at redshift $z = 0$.

In the second set of simulations we have used a box of width $16h^{-1}$ Mpc. These simulations are used to study the cumulative halo mass function and the redshift evolution of halo abundances. This approach provides a better force and mass resolution, but due to smallnes of the box we lack some power in large-scales. For a discussion of the influence of the box-size on the dynamics and statistics of simulations, see Ref. [24, 25].

In each experiment we save the particle positions and velocities at redshifts 5; 2; 1; 0.5; 0.3; 0.2; 0.1; 0.05, and the reshift of the final output, $z = 0$. This archive is used to study the evolution of the dark matter distribution with reshift. For an experiment, involving N_p dark matter particles in a box of size L at present, the particle mass, m_p, is given by

$$m_p \;=\; \langle\rho\rangle\;(L^3/N_p). \tag{15}$$

For our simulations, $N_p = 128^3$. The other important simulation parameters are: the force resolution ε, the interparticle separation,

$$\ell \;=\; (L^3/N_p)^{1/3} \;\;, \tag{16}$$

and the Nyquist wavenumber,

$$k_{\rm Nyq} \;=\; \pi/\ell \;\;. \tag{17}$$

We list the above parameters, evaluated for the large and the small box, in Table I.

C. The Green's Function

For conventional gravity in Fourier space, the discrete Poisson equation can be written as

$$\phi_{\mathbf{k}} \;=\; \frac{3H_0^2\Omega_M}{2a}\,\delta_{\mathbf{k}}\,\mathcal{G}_{\mathbf{k}}\,, \tag{18}$$

where $\mathcal{G}_{\mathbf{k}}$ is the Green's function. We use the seven-point finite-difference approximation to the Green's function to solve the Poisson's equation in a cubic box with periodic boundary conditions. It is defined for a discrete set of arguments,

$$\mathbf{q} \;=\; \{q_j\} \;=\; \mathbf{k}\cdot L/(2\pi)\,, \tag{19}$$

where L is the present size of the comoving simulation box. The subscripts $j = 1, 2$ or 3 denote the three dimensions in $\mathbf{k}$-space. The number of grid cells in each dimension is $\mathcal{N}$ (256 in our simulations), so the cell numbers assume integer values in the range

$$q_j \;=\; 1, 2, \ldots, \mathcal{N}\,. \tag{20}$$

Each integer triple defines the grid point, at which the Green's function is evaluated:

$$\mathcal{G}^{\rm N}_{\mathbf{q}} = -\pi\left[\mathcal{N}^2\sum_{j=1}^{3}\sin^2(\pi q_j/\mathcal{N})\right]^{-1}\;. \tag{21}$$

Using the equation. (6), we modify Green's function to get the proper potential for our model of scalar interactions:

$$\mathcal{G}^{\rm scalar}_{\mathbf{k}} = \mathcal{G}^{\rm N}_{\mathbf{k}}\;\left(1+\frac{\beta}{1+(kr_s)^{-2}}\right)\;. \tag{22}$$

The AMIGA code uses equation (18) and the fast Fourier transform technique to evaluate the gravitational potential at grid points. Then particle positions and momenta are updated in the standard way for PM algorithms.

D. Particles and Halos

To identify collapsed objects from now on called 'halos' we have used AMIGA's Halo Finder (AHF) which is the most recent version of MHF halo finder by Gill, Knebe & Gibson [26]. The AHF uses AMR to find halo centers, then it probes the halo density profile around each center in nested radial bins until the spatially averaged density contrast reaches the virial overdensity, Δ. At $z = 0$, in a ΛCDM universe [27], $\Delta = 340$. Given our mass resolution in the bigger box, we can expect to follow the assembly of halos, corresponding to clusters and superclusters, and study the statistics of clustering at large scales. Simulations in the small box should be good enough to investigate the assembly of much less massive objects, like halos of clusters, galaxies and groups of galaxies.

It is important to bear in mind that at small scales we are limited by poor force resolution. The smallest size of gravitationally bound objects which can form in our box is 2ε (see Table 1 and Ref. [28]). We allso suffer from the well-known problem of *overmerging* described in great detail by Klypin et al. in Ref. [29]. As a consequence, our simulations underestimate low-mass object abundances.

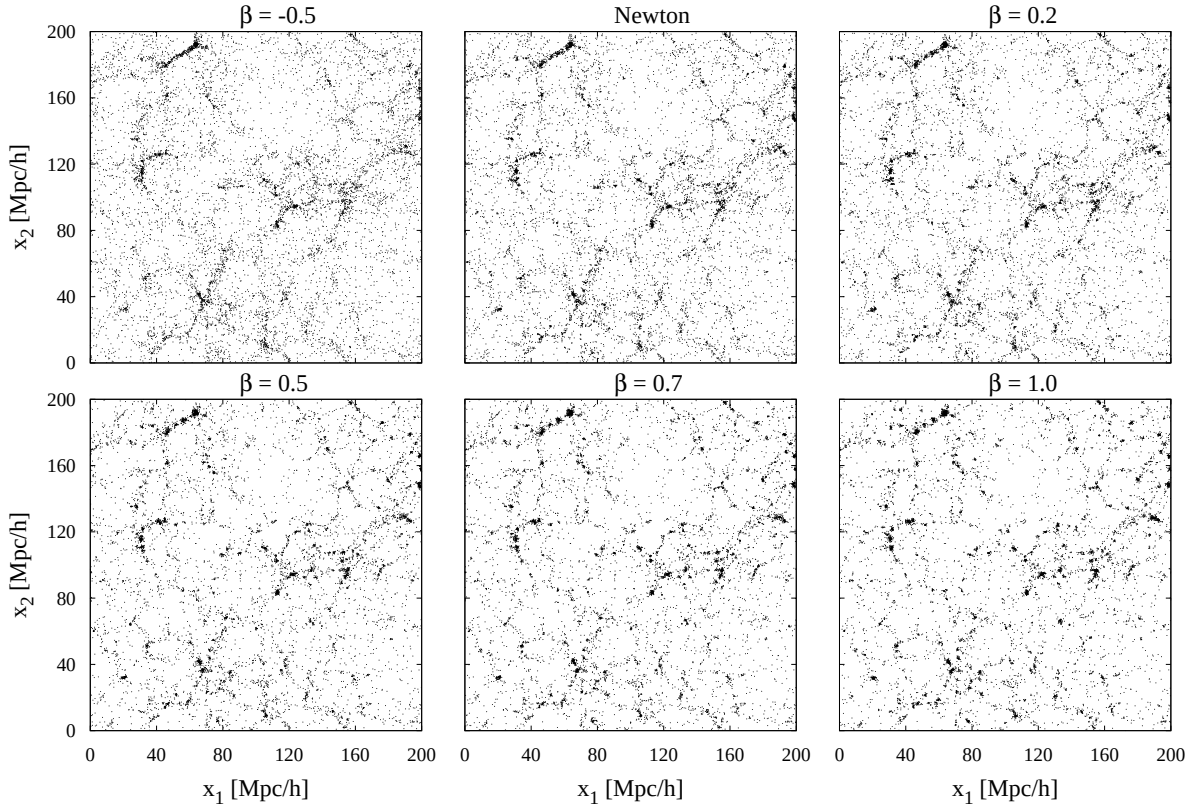

FIG. 1: Slices cut through centers of simulation boxes of width $200h^{-1}$ Mpc at $z = 0$. The plots show particle positions, $\mathbf{x}$, in the (x_1, x_2) plane. Each slice has dimensions $200 \times 200(h^{-1}\,\mathrm{Mpc})^2$ in this plane and a thickness of $10h^{-1}$ Mpc along the x_3 coordinate axis.

TABLE I: Simulation parameters. L is the box size $[h^{-1}\,\mathrm{Mpc}]$; z is the initial redshift; m_p is the mass of a single particle $[h^{-1}M_S]$; ε is the force resolution $[h^{-1}\,\mathrm{kpc}]$; ℓ is the mean interparticle separation $[h^{-1}\,\mathrm{Mpc}]$; k_{Nyq} is the Nyquist wavenumber $[h\mathrm{Mpc}^{-1}]$; $N.R.$ is the number of realizations for each pair of r_s and β; r_s is the screening length $[h^{-1}\,\mathrm{Mpc}]$; β is the relative strength of the scalar force.

L	z	m_p	ε	ℓ	k_{Nyq}	$N.R.$	r_s	β
200	30	$3.18 \cdot 10^{11}$	800	1.563	2.01	10	$1; 2; 5$	$-0.5; 0; 0.2; 0.5; 0.7; 1$
16	40	$1.60 \cdot 10^{8}$	70	0.125	25.1	5	$1; 2$	$0; 0.2; 0.5; 1$

IV. RESULTS

In this section we present the results obtained in our numerical experiments. We provide maps of the spatial distribution of dark matter particles as well as clumps of particles, called halos. We also study different statistical measures of clustering, such as the power spectrum, the two-point correlation function and the cumulative halo mass function with and without the scalar interaction.

A. The Clustering Pattern

Figure 1 shows the final particle distribution in $10h^{-1}$ Mpc slices, cut through the centers of $200h^{-1}$ Mpc simulation boxes. For clarity each slice shows only 1/10 of the total number of particles, selected at random [40]

The frame, labeled 'Newton' in Figure 1 assumes $\beta = 0$, while the remaining frames show particle distributions for a set of different β parameters and a fixed screening length, $r_s = 2h^{-1}$ Mpc. As a test, we also consider 'anti-gravity' with $\beta = -0.5$. All of the frames in Figure 1 have evolved from the same initial state, with identical amplitudes and phases of density fluctuations, set up at $z = 30$.

At first sight, modified gravity simulations look similar to the Newtonian case. The filaments, voids and high-density peaks occupy similar positions in the frames. However, a close inspection shows that with increasing β, the voids appear increasingly more empty. This phenomenon is seen more clearly in Figure 2, where we show $2h^{-1}$ Mpc slices, cut through the centers of our smaller simulation boxes ($L = 16h^{-1}$ Mpc).

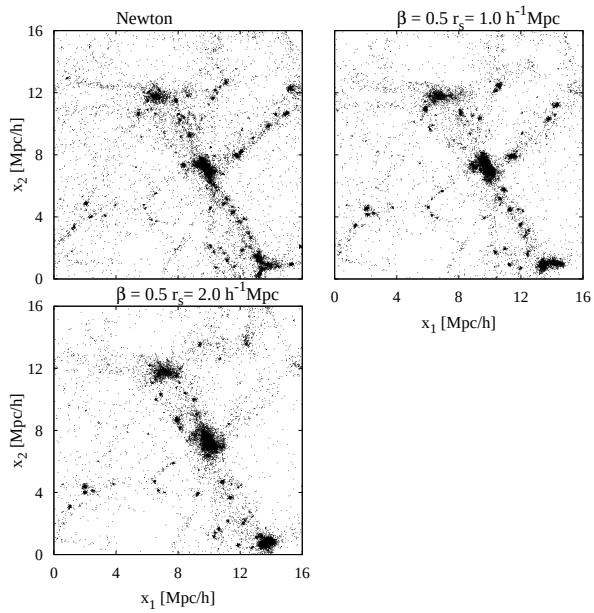

FIG. 2: Similar results for the smaller box, $L = 16h^{-1}$ Mpc. The thickness of each slice is $2h^{-1}$ Mpc.

Figure 2 also shows that the scalar forces enhance the accretion of matter, producing more massive halos at small scales. Pancake-like structures, seen in the $\beta = 0$ frame, are more homogeneous than their counterparts in frames with $\beta > 0$, which show substructure. The fragmentation into subsystems of smaller halos is increasingly more pronounced, with increasing values of β. Quantitatively, we can expect an increase of the amplitude of the power spectrum at small scales, corresponding to wavenumbers $k \gtrsim r_s^{-1}$, and an opposite effect for $\beta = -0.5$, when the pancakes appear even more homogeneous than those generated by Newtonian gravity.

B. The Power Spectrum

The power spectrum is a convenient measure of the strength of dark matter clustering. It is well constrained by redshift surveys of galaxies, such as the SDSS catalog [41]. In the longwave tail, corresponding to wavenumbers

$$0.01\,\mathrm{Mpc}^{-1}h \;\leq k \;\leq\; 0.3\,\mathrm{Mpc}^{-1}h \;\;, \qquad (23)$$

this survey provides a reliable estimate of $P(k)$ [30]. In this range, the ΛCDM power spectrum agrees well with observations. This can be used to constrain scalar field models.

In Figure 3 we plot the final power spectra, obtained from the simulations with $L = 200h^{-1}$ Mpc. The top pair of plots shows $P(k)$ and the ratio P/P_{N} for scalar forces with fixed $\beta = 0.5$ and a varying screening length. The pair of plots below was obtained from simulations with a fixed screening length, $r_s = 1h^{-1}$ Mpc, and a varying β.

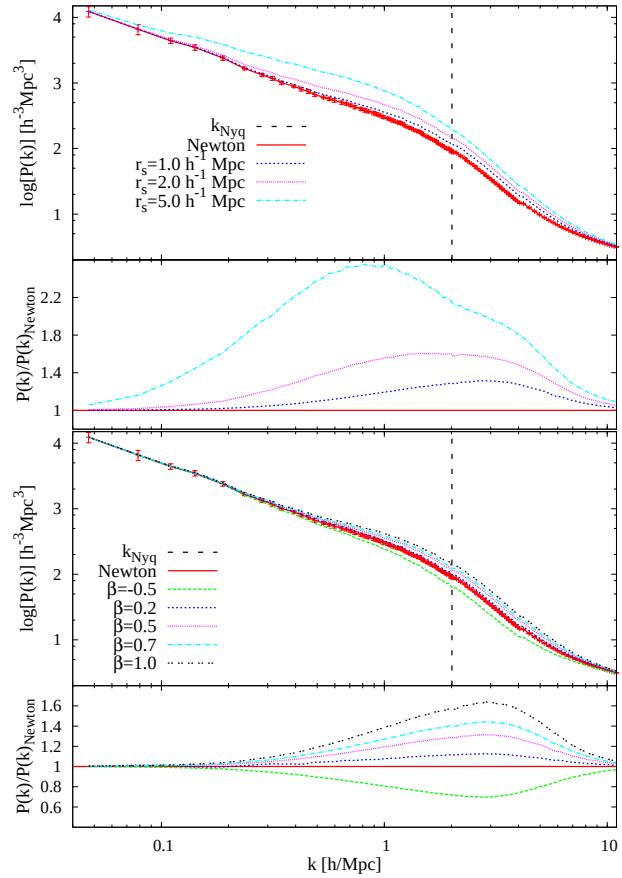

FIG. 3: Power spectra from simulations with $L = 200h^{-1}$ Mpc. Vertical dashed lines show the Nyquist wavenumber. We also plot the ratio of the scalar interaction induced $P(k)$ to its Newtonian counterpart, $P_{\mathrm{N}}(k)$. For all of the upper pair of plots $\beta = 1$, while the r_s paremeter is allowed to vary. For the bottom pair $r_s = 1h^{-1}$ Mpc is fixed, while the value of β changes from -0.5 to 1. Each curve was obtained by averaging over 10 simulation realizations with different initial phases.

These plots show that the rate of growth of density perturbations is more sensitive to the range of the scalar field, r_s, than to its strength, as long as $\beta > 0$. The scalar force increases the rate of growth of density fluctuations on comoving scales, smaller than r_s and wavenumbers $k \gtrsim r_s^{-1}$. As expected, there is an opposite effect for $\beta = -0.5$: the rate of growth of density perturbations at small scales is reduced.

We describe the deviations from the Newtonian power spectrum at a given wavenumber by the parameter

$$\frac{\Delta P}{P} \equiv \frac{P - P_{\mathrm{N}}}{P_{\mathrm{N}}} \quad . \qquad (24)$$

These deviations remain negligible on large scales for all of the considered models with one exception: the model with $r_s = 5h^{-1}$ Mpc. For this model, $\Delta P/P$ is significant on all scales present in simulation box, including the SDSS wavenumber range. Therefore all scalar field models with $r_s \geq 5h^{-1}$ Mpc do not appear promising.

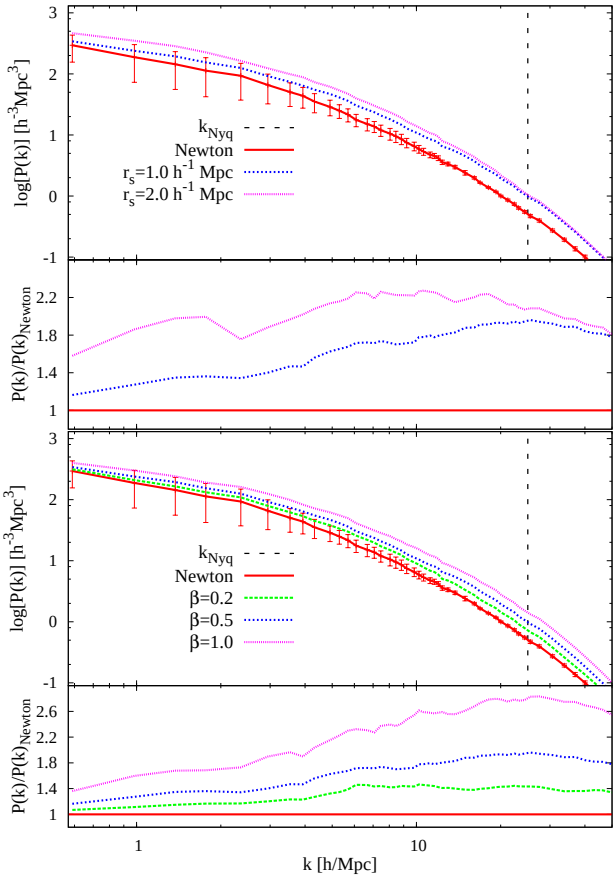

FIG. 4: Power spectra plots similar to those in figure 3, obtained from a set of simulations, using the smaller box, $L = 16h^{-1}$ Mpc. Each curve shown here is an average over 5 realizationrealizations with different initial phases.

To assign statistical significance to their failure to reproduce the real Universe, it is necessary to create a mock SDSS survey and reproduce the power spectrum estimator, used by the observers. We are planning to run appropriate Monte Carlo simulations and address this problem in greater detail in a forthcoming paper.

The model with $r_s = 5h^{-1}$ Mpc may not be successful in reproducing the real Universe, but it is extremely useful in understanding the physics of the scalar field because this value of the screening length is much larger than the interparticle separation in the big box, $\ell \approx 1.6h^{-1}$ Mpc. Therefore, we can resolve the difference between purely Newtonian gravity and the scalar field. Indeed, for $k = 1/r_s = 0.2$, and $\beta = 0.5$, we get $\Delta P/P = 0.5$ (see Figure 3), and an increasing $\Delta P/P$ for larger wavenumbers. The gravitational attraction, enhanced by the scalar field generates the extra power in the plot. To look for a similar jump in amplitude for smaller values of r_s, we need a better resolution. So, we have to turn to the simulations in the smaller box, where $\ell = 125h^{-1}$ kpc. And we do find a similar feature: for $\beta = 0.5$ and $r_s = 1h^{-1}$ Mpc, we get $\Delta P/P = 0.5$ at $k = 1/r_s = 1h\mathrm{Mpc}^{-1}$ (see Figure 4)!

The decline of $P_{\rm N}/P$ with decreasing wavenumber in all considered models is a natural consequence of the presence of the Yukawa cutoff, reflected in the equation (11).

In the opposite limit, with growing wavenumbers, all power spectra in Figure 3 seem to misbehave. Equation (13) suggests that all $P_{\rm N}/P$ curves should flatten for large wavenumbers, $k \gg 1/r_s$. Instead, we see a decline. Since this behavior is in disagreement with gravitational dynamics, and since it appears in the range $k \gtrsim k_{\rm Nyq}$, we can expect that the decline is an artifact of the discrete nature of the simulation. If this is indeed the case, then in the simulation in the smaller box, this artifact should move to higher wavenumbers. This simulation has a smaller interparticle separation and a better force resolution. Hence, for wavenumbers in the range

$$r_s^{-1} \lesssim k \lesssim k_{\rm Nyq} \ , \tag{25}$$

we should see a flat section of the $P/P_{\rm N}$ curve, followed by a decline for $k \gtrsim k_{\rm Nyq}$. This is exactly what happens in Figure 4. The $P_{\rm N}/P$ ratio rises with k until it reaches its maximum, followed by a plateau, and then by decline for wavenumbers above the Nyquist limit.

C. The Correlation Function

Another convenient measure of the strength of clustering is the spatial two-point correlation function,

$$\xi\ (|\mathbf{x}-\mathbf{x}'|,\, t) \ = \ \langle\, \delta(\mathbf{x},t)\delta(\mathbf{x}',t)\,\rangle \ . \tag{26}$$

It is related to the power spectrum by the Fourier transform,

$$\xi\,(x) \ = \ (2\pi)^{-3} \int P(k)\, e^{i\mathbf{k}\cdot\mathbf{x}}\, d^3\mathbf{k} \ . \tag{27}$$

Under ideal conditions, when the power spectrum is determined in the entire wavenumber range from zero to infinity, P and ξ are equivalent to each other. However, measurements from simulations or galaxy redshift surveys provide only noisy estimates of $P(k)$ or $\xi(x)$ for limited ranges of k and x. Therefore, in numerical experiments, it is safer to estimate $\xi(x)$ directly from the particle positions in the simulation output, using the expression (26), or its discrete version, based on the probability density of finding a pair of particles in a separation range from x to $x + dx$ (see Ref. [12]). The results presented in this section are therefore not a mere Fourier transform of the results discussed in two previous subsections. Following the approach we used to study power spectrum deviations from the Newtonian case, here we introduce a similar measure of the deviations of the scalar-induced correlation function from its Newtonian cousin, $\xi_{\rm N}$. This is the quantity

$$\frac{\Delta\xi}{\xi} \ \equiv \ \frac{\xi - \xi_{\rm N}}{\xi_{\rm N}} \ . \tag{28}$$

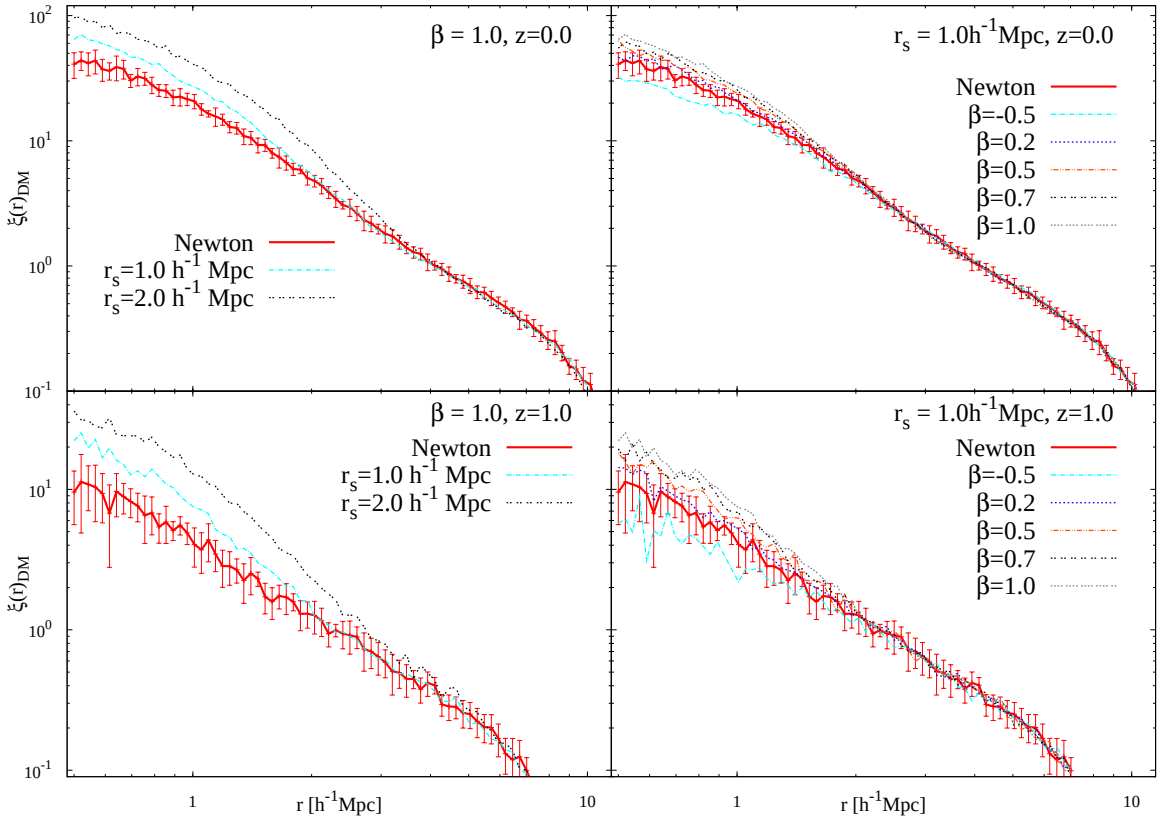

FIG. 5: The correlation function for pairs of DM particles at redshift z = 1 (bottom frames) and z = 0 (top frames). The width of the simulation box is $200h^{-1}$ Mpc. All plots were averaged over 10 simulations. To avoid overcrowding, we show one standard deviation error bars for the Newtonian $\xi(x)$ only. The error bars for the scalar induced correlation functions are similar. Their size is determined mostly by the number of realizations and by the size of the box. Both these quantities are identical for all simulations presented here.

The four frames in Figure 5 show two-point correlation functions for DM particles in the $200h^{-1}$ Mpc box. The top two frames show simulation outputs at $z = 0$, while the bottom frames refer to an earlier epoch, $z = 1$. For clarity, we show one standard deviation errors only for the Newtonian case. The error bars for the remaining models are similar.

The large amplitude in $\Delta\xi/\xi$ at separations $x \lesssim 1h^{-1}$ Mpc is probably an artifact because the separations involved are smaller than $\ell = 1.56h^{-1}$ Mpc. Nusser et al. [3] have discovered a similar shoulder in $\xi(x)$ in their simulations and they provided an interpretation similar to ours. They have also pointed out that the correlation function in their simulations does not possess a feature at $x = r_s$ "despite the scalar force attraction at smaller scales". We believe that the source of this problem is poor resolution, not dynamics. The range of screening lengths they consider is uncomfortably close to their interparticle separation. Our correlation functions, plotted in Figure 5 suffer from the same problem. As we have shown in our discussion of the properties of simulated power spectra, this problem can be avoided by improving the resolution. For an appropriate choice of the box size and the screening length, when $r_s > 1/k_{\rm Nyq}$, the feature at $k = 1/r_s$ can be resolved. We therefore have no doubt - the feature is there. To rediscover for $\xi(x)$ what we have already seen for $P(k)$, we only need higher resolution simulations, like those in Ref.[31], but with a modified Green's function.

Despite the modest resolution of the present results, we believe that qualitatively, the stratification of the correlation functions with respect to r_s and β, seen in Figure 5 reflect the true dynamics. Note that for $\beta < 0$, when gravity is weaker than Newtonian, we get $\Delta\xi/\xi < 0$, which is dynamically reasonable.

Our results also differ from those of Nusser et al. at larger separations, $x > 3h^{-1}$ Mpc, where according to their Figure 7, $\Delta\xi/\xi < 0$. This does not happen in our simulations unless $\beta < 0$. This discrepancy, however, becomes statistically insignificant if we use our error bars for guidance (Nusser et al. do not provide error bars for their plots).

As we already mentioned, for separations $x > r_s$, $\Delta\xi/\xi$ is consistent with zero for all models considered here. This is good news, since the observed $\xi(x)$ at large separations agrees well with the ΛCDM model.

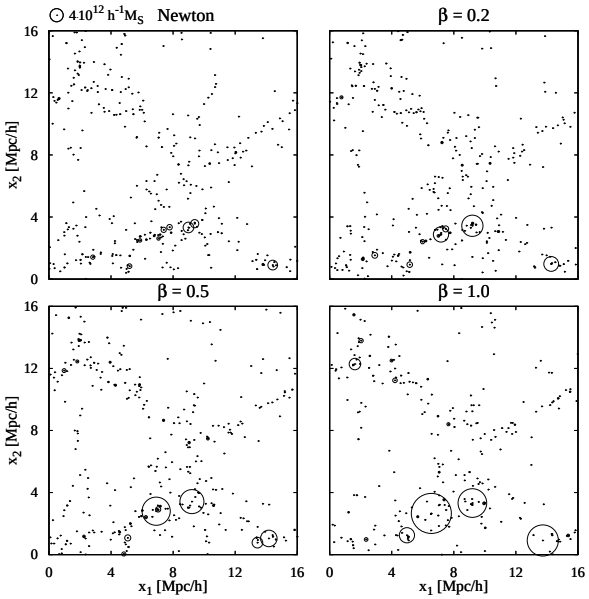

FIG. 6: Positions of halo centers obtained from particular simulation output. The size of the box is $L = 16h^{-1}$ Mpc. To avoid overcrowding, we show only the halos with centers in the range $0 \leq x_3 \leq 8h^{-1}$ Mpc. Halos with masses greater than $1.15 \cdot 10^{12} M_\odot$ appear as circles. Their diameters are proportional to their masses. Less massive halos are represented by dots. The top left frame shows the standard gravity case. The halo distribution in all of the remaining frames is plotted for $r_s = 1h^{-1}$ Mpc and three different values of β. For reference, above the upper frame on the left we show a circle, representing a halo with a mass of $4 \cdot 10^{12} M_\odot$.

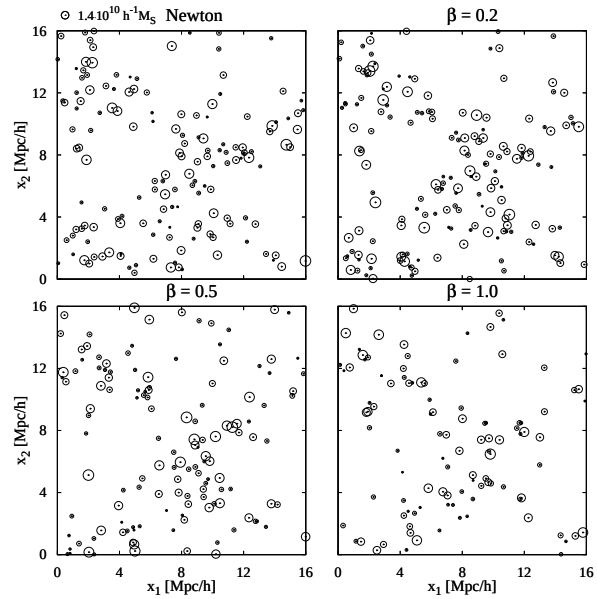

FIG. 7: Maps of the halo distribution, derived from the same simulations as those shown in Figure 6, but for halos with masses, smaller than $\mathtt{M} = 2 \cdot 10^{10} h^{-1} M_\odot$. Even smaller halos with masses $M \leq \mathtt{m} = 7 \cdot 10^9 h^{-1} M_\odot$ are represented by dots. Those with masses in the range $\mathtt{m} < M \leq \mathtt{M}$ appear as circles.

Last but not least, it is worth noticing that in Figure 5, $\Delta\xi/\xi$ is higher at $z = 1$ than at $z = 0$. The growth of Newtonian ξ is retarded with respect to the scalar-induced ξ at high redshift. Later, $\xi_{\rm N}$ 'catches up' with the scalar ξ. As a consequence, $\Delta\xi/\xi$ is reduced. A possible explanation for this phenomenon is that in the presence of scalar forces, rapid matter accretion and formation of virialised objects occurs at earlier epochs than in the standard gravity model. This interpretation is supported by our direct analysis of the process of halo formation, presented below.

D. Forming Halos in a Small Box

In this section we study the impact of modified gravity on the halo formation process. To identify halos, we apply the halo finder program (the `AHF`, introduced earlier) to output snapshots from the $16h^{-1}$ Mpc simulations. We study all halos with more than 20 particles, hence our minimal halo mass is $3.2 \cdot 10^9 h^{-1} M_\odot$.

1. *High Mass Halos*

In Figure 6 we plot the present comoving positions $\mathbf{x} = (x_1, x_2, x_3)$ of halo centers in the (x_1, x_2) coordinate plane of the simulation box. To avoid overcrowding, we consider only halo centers which satisfy the condition $0 \leq x_3 \leq 8h^{-1}$ Mpc. Halos with masses exceeding $\mathtt{M} = 1.15 \cdot 10^{12} h^{-1} M_\odot$ are plotted as circles with diameters proportional to halo masses. For reference, the size of a circle, representing a halo with a mass of $4 \cdot 10^{12} M_\odot$ is shown in Figure 6, above the upper left frame. The halos with masses $M < \mathtt{M}$ are plotted as dots. It is interesting to note that as expected, the scalar interactions enhance the ability of the larger halos to accrete matter and become even larger. This effect is particularly striking when we compare the upper left, Newtonian frame, with the lower right frame where $r_s = 1h^{-1}$ Mpc and $\beta = 1$. The halos seen in the rectangle

$$6.0h^{-1}\,\mathrm{Mpc} \;<\; x_1 \;< 10h^{-1}\,\mathrm{Mpc} \;, \tag{29}$$

$$2.0h^{-1}\,\mathrm{Mpc} \;<\; x_2 \;< 4.0h^{-1}\,\mathrm{Mpc} \;, \tag{30}$$

at lower right have already acreted all debris in their vicinity at earlier times, while in the Newtonian frame the accretion process is still going on. At the same time, the small-scale mass redistribution process does not affect the large-scale clustering: the cosmic web is clearly visible in all of the frames. An example of this is the cosmic wall, extending diagonally across the simulation box from the origin of the coordinate system, $(0, 0)$, to $(16h^{-1}\,\mathrm{Mpc}, 12h^{-1}\,\mathrm{Mpc})$.

2. Low Mass Halos

In this section we look at the low mass end of the halo population. Our Figures 7 and 6 are complementary to each other. Both are derived from the same simulation, except this time we show only halos with masses $M \leq \mathtt{m} = 2 \cdot 10^{10} h^{-1} M_\odot$. The circles show halos with masses $7 \cdot 10^9 h^{-1} M_\odot \leq M \leq \mathtt{m}$. The remaining halos, with masses $M \leq 7 \cdot 10^9 h^{-1} M_\odot$, are plotted as dots. As before, the diameters of the circles are proportional to halo masses. The influence of the scalar field is particularly well pronounced when we compare frames with scalar field switched off ($\beta = 0$, upper left) and on ($\beta = 1$, lower right). The low abundance of light halos, seen here, is consistent with the high abundance of heavy halos in Figure 6. Both Figures show the rapid accretion and massive halo formation at high redshift, induced by the scalar force.

3. The Cumulative Mass Function

For a more quantitative description of the halo formation process, we will now introduce the cumulative mass function (cmf), defined as the mean number density of halos with masses greater than the argument mass,

$$n(> M) \;=\; \frac{N_H(> M)}{L^3} \;, \tag{31}$$

where $N_H(> M)$ is the number of halos with masses greater than M, identified within the a comoving volume L^3. The mean is obtained by averaging $N_H(> M)$ over five simulations. Later we will also consider the mean number density of halos below a certain mass threshold, $n(< M)$. The sum of these two densities, multiplied by L^3 gives the mean number of halos of all masses.

In Figure 8 we show the redshift evolution of the cmf for several models. The comparison of the Newtonian cmf with its scalar counterparts confirms the results obtained by plotting the positions of halos with different masses. All scalar models show enhanced abundances of high mass halos and reduced abundances of low mass halos at $z = 0$. For $r_s = 2h^{-1}$ Mpc, the low mass tail of the cmf drops by almost an order of magnitude below the Newtonian cmf. To show this in greater detail, we plot a magnified picture of low mass tails of all histograms at $z = 0$ in Figure 9. The reduction of low mass halo abundances is encouraging in the light of the missing-satellites problem [32, 33, 34]. The upper left frame in Figure 8 shows another interesting property of the models we consider here. For halo masses in the galactic range, $10^{11} M_\odot$ to $10^{12} M_\odot$, the scalar-induced halo abundances agree with the Newtonian predictions. This is an advantage because the galactic number densities predicted by the ΛCDM model agree with observations [35].

Another interesting phenomenon is the overproduction high mass halos in the cluster mass range, $M \sim 10^{13} h^{-1} M_\odot$. The cluster abundance at $z = 0$ is relatively well known from observations and it provides a strong cosmological test. It has been used in the past to exclude the once popular Einstein-de Sitter CDM model (Peebles et al. 1989). To decide how deadly this may become for scalar interaction models, we need a larger box to sample the cluster population properly and more particles to keep a reasonable force resolution. Clusters are rare objects. In a $16h^{-1}$ Mpc box, at the cluster mass range, we are dominated by small-number statistics. The mean distance between a pair of ΛCDM clusters (as well as real clusters in galaxy surveys) is $\sim 50h^{-1}$ Mpc. Nusser et al., who used a $50h^{-1}$ Mpc box, found only a small excess of the scalar-induced cluster halo abundance over the Newtonian case. We plan to study this problem, using higher resolution simulations in the nearest future.

Apart from plotting $n(> M)$ as a function of M for fixed redshifts, it is also interesting to fix the mass and see how the cmf evolves with z. In Figure 10 we present the redshift evolution of two measures of halo abundances, $n(\leq 10^{10} h^{-1} M_\odot)$, shown on the left, and $n(\geq 10^{11} h^{-1} M_\odot)$, shown on the right.

Note that for all scalar models, the low mass halo abundances are higher than in the Newtonian case at high redshift. This happens because the enhanced gravity at small scales speeds up the halo formation process. For the same reason, these abundances drop below the Newtonian values with decreasing redshift. The light halos become extinct because they merge with larger mass halos. This process is responsible for evacuating the voids more effectively than conventional Newtonian forces.

On the high mass end, we see two interesting effects:

First, because of faster accretion, the higher mass halos reach abundances, close to their final values at relatively high redshifts. Later, their number densities change less rapidly with reshift than the Newtonian halo number density. This is particularly prominent in the right frame at the bottom of Figure 10. Such a picture is consistent with the observational evidence for an uneventful recent past of galaxies like our Milky Way and other nearby galaxies, allowing merger events only at high reshifts [36, 37, 38]. In contrast, for the Newtonian model, we see rapid growth of $n(\geq 10^{11} h^{-1} M_\odot)$ with decreasing redshift, suggesting that mergers continue to the present day.

The second effect, particularly pronounced in the right frame at the bottom of Figure 10, is the convergence of all of the $n(> M)$ curves at $z = 0$. Since our mass threshhold for this set of cumulative mass functions is in the galactic mass range, this convergence is a promising feature of scalar models, because the ΛCDM abundance of galaxies agrees with observations [39].

E. The most massive halo

We finish by showing the impact of attractive scalar forces on the properties of most massive particle concen-

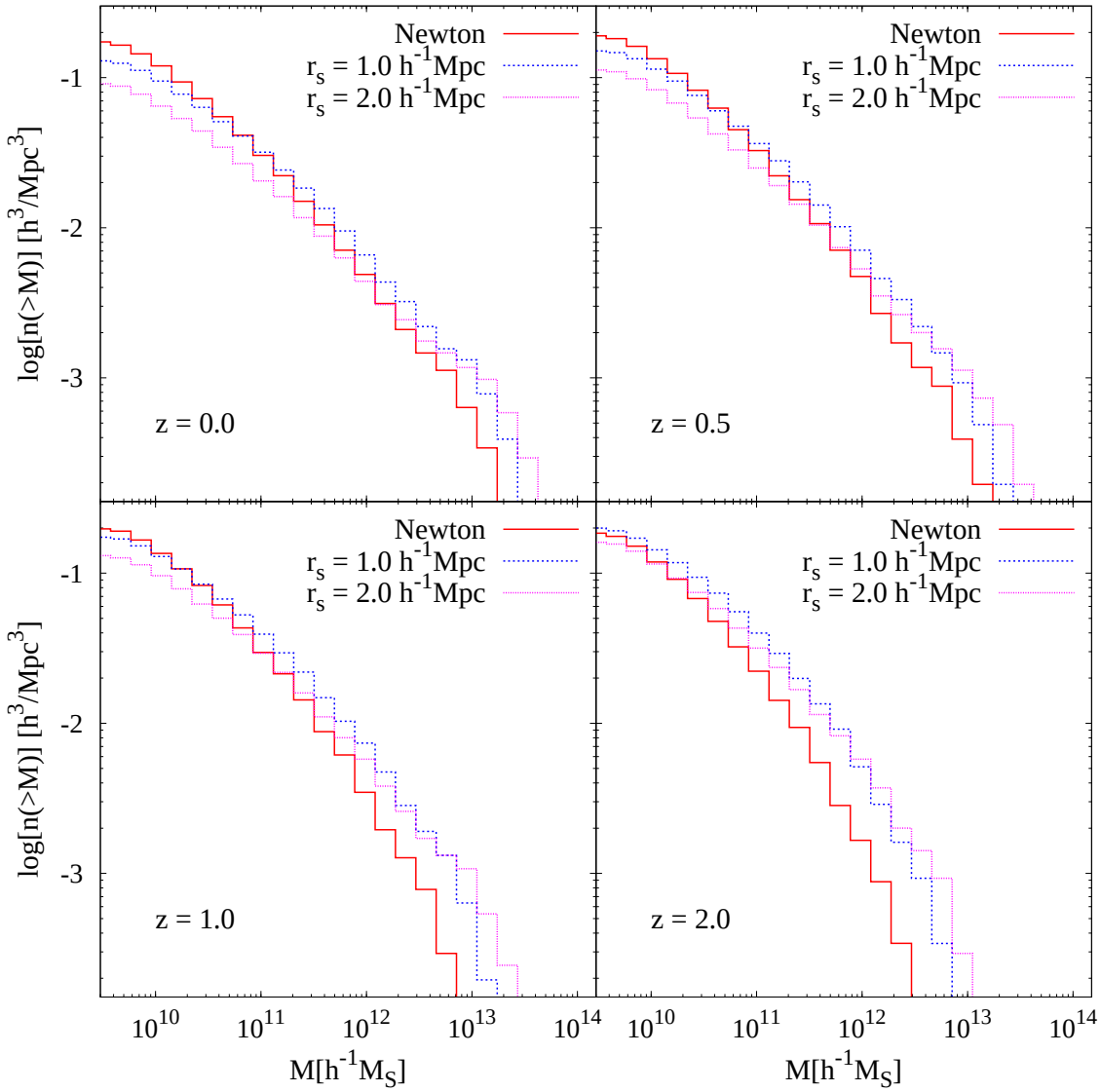

FIG. 8: The redshift evolution of the cumulative halo mass functions in simulations with $L = 16h^{-1}\,\mathrm{Mpc}$. We show the Newtonian case and two scalar models with $\beta = 1$ and two different values of r_s. Each curve was obtained by averaging 5 simulations with different initial phases.

TABLE II: Averaged properties of the most massive halo found in a simulation box of width $16h^{-1}$ Mpc. Gravity models are parameterized by β and r_s in h^{-1} Mpc; M is the halo mass; σ_v is the velocity dispersion; r_{vir} is the virial radius. The first row, with the vanishing β and r_s, represents ΛCDM cosmology with Newton's gravity.

β	r_s [h^{-1} Mpc]	$M/10^{13}M_\odot$	σ_v [kms^{-1}]	r_{vir} [h^{-1} kpc]
0.0	0.0	3.4 ± 2.2	494 ± 110	630 ± 135
0.2	1.0	3.6 ± 2.5	565 ± 161	644 ± 138
0.2	2.0	4.5 ± 2.4	604 ± 102	702 ± 125
0.5	1.0	4.0 ± 2.4	646 ± 118	673 ± 130
0.5	2.0	5.2 ± 2.6	732 ± 113	739 ± 119
1.0	1.0	4.7 ± 2.8	780 ± 162	706 ± 135
1.0	2.0	7.3 ± 3.7	984 ± 180	845 ± 137

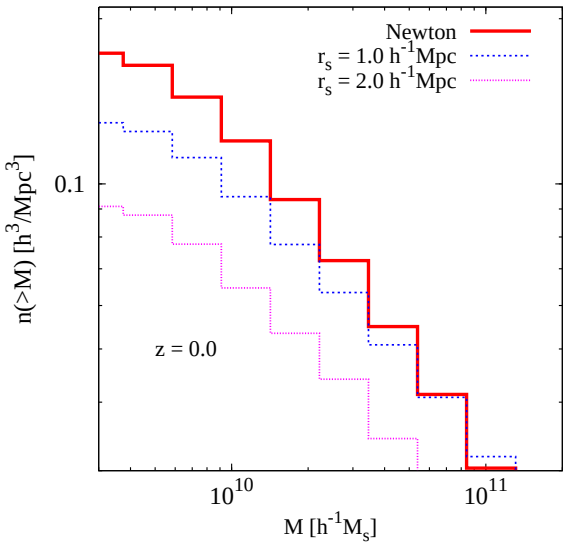

FIG. 9: A magnified section of Figure 8, taken from the $z = 0$ frame, showing low-mass tails of cumulative mass functions.

trations in the box. In table II we list average properties of the most massive halo in our $16h^{-1}$ Mpc simulations. These results were obtained by averaging over five realizations with different initial phases for each pair of β and r_s. The mass, velocity dispersion and the virial radius of the most massive member of the halo population increase with increasing r_s and β, as expected.

V. SUMMARY

We have performed N-body simulations of large scale structure formation in a ΛCDM background, with a Newtonian potential, modified by the scalar interaction. We have studied the spatial distribution of dark matter particles and halos. We also investigated statistical measures of clustering, such as the two-point correlation function, the power spectrum, and the cumulative halo mass function. We find that the scalar interaction removes debris from cosmic voids more effectively than the standard ΛCDM model. It also suppresses late accretion and merger activity; halo formation processes move to higher redshifts. These findings agree very well with earlier work [3]. For the first time in the literature, we have also shown the effect of scalar forces on the evolution of the power spectrum. We have resolved the boundary between pure Newtonian dynamics, and enhanced power, generated by the scalar interactions.

In the near future we plan to run higher resolution simulations. We will follow the evolution of the baryon spatial distribution, as well as the dark matter. We will also consider the three-point correlation function and bispectrum - statistics of higher order, than those considered here. Finally we expect to constrain the scalar field parameter range by direct comparisons of model predictions with observations.

Acknowledgments

This research was partially supported by the Polish Ministry of Science Grant no. NN203 394234. WAH would like to thank Alexander Knebe, Pawel Ciecielag, Michal Chodorowski and Radek Wojtak for valuable discussions and comments. Simulations presented in this work were performed on 'PSK' cluster at NCAC.

[1] D. N. Spergel, R. Bean, O. Doré, M. R. Nolta, C. L. Bennett, J. Dunkley, G. Hinshaw, N. Jarosik, E. Komatsu, L. Page, et al., Astrophys. J. Suppl. Ser. **170**, 377 (2007), arXiv:astro-ph/0603449.
[2] P. J. E. Peebles, Astrophys. J. **557**, 495 (2001), arXiv:astro-ph/0101127.
[3] A. Nusser, S. S. Gubser, and P. J. Peebles, Phys. Rev. D **71**, 083505 (2005), arXiv:astro-ph/0412586.
[4] P. J. Peebles and B. Ratra, Rev. Mod. Phys. **75**, 559 (2003), arXiv:astro-ph/0207347.
[5] G. R. Farrar and P. J. E. Peebles, Astrophys. J. **604**, 1 (2004), arXiv:astro-ph/0307316.
[6] T. Battefeld and S. Watson, Rev. Mod. Phys. **78**, 435 (2006), arXiv:hep-th/0510022.
[7] M. A. Rodríguez-Meza, A. X. González-Morales, R. F. Gabbasov, and J. L. Cervantes-Cota, J. Phy. Conference Series **91**, 012012 (2007).
[8] M. A. Rodríguez-Meza, in *Recent Developments in Gravitation and Cosmology* (2008), vol. 977 of *American Institute of Physics Conference Series*, pp. 302–309.
[9] J. L. Cervantes-Cota, M. A. Rodríguez-Meza, and D. Nuñez, J. Phys. Conference Series **91**, 012007 (2007), arXiv:0707.2692.
[10] S. S. Gubser and P. J. E. Peebles, Phys. Rev. D **70**, 123510 (2004), arXiv:hep-th/0402225.
[11] S. S. Gubser and P. J. E. Peebles, Phys. Rev. D **70**, 123511 (2004), arXiv:hep-th/0407097.
[12] P. J. E. Peebles, *The large-scale structure of the universe* (Research supported by the National Science Foundation. Princeton, N.J., Princeton University Press, 1980. 435 p., 1980).
[13] G. Dvali, G. Gabadadze, and M. Porrati, Phys. Lett. B **485**, 208 (2000), arXiv:hep-th/0005016.
[14] S. Nojiri and S. D. Odintsov, ArXiv e-prints (2006), hep-th/0601213.
[15] C. Sealfon, L. Verde, and R. Jimenez, Phys. Rev. D **71**, 083004 (2005), arXiv:astro-ph/0404111.
[16] A. Shirata, T. Shiromizu, N. Yoshida, and Y. Suto, Phys. Rev. D **71**, 064030 (2005), arXiv:astro-ph/0501366.

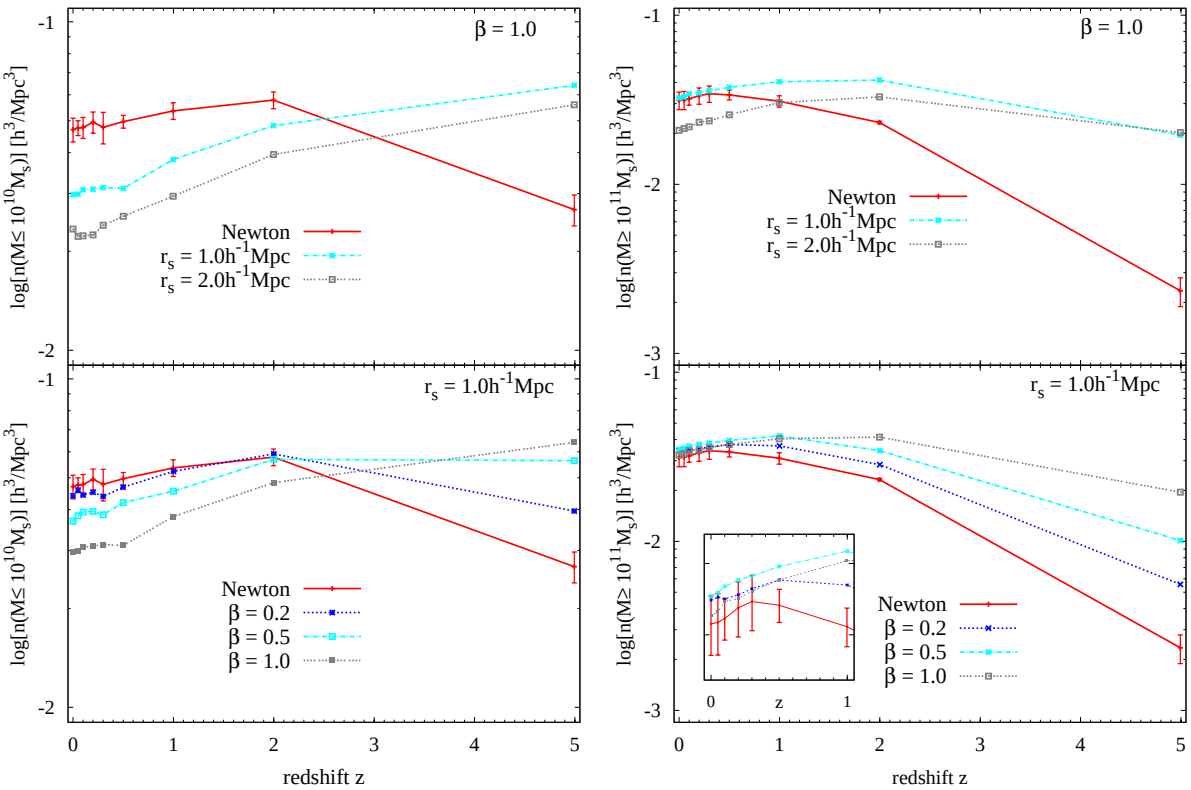

FIG. 10: Redshift evolution of the abundance of halos. On the left, we show the low mass end of the distribution, $n(M) \leq 10^{10}h^{-1}M_{\odot}$. The frames at the right describe the halo population with higher masses, $n(M) \geq 10^{11}h^{-1}M_{\odot}$. The small box inset in the bottom right frame is a magnification of the $0 \leq z \leq 1$ region in the same frame. Each curve is a result of averaging over 5 simulations. For clarity we present one sigma error bars for the Newtonian $n(< M)$ plots only.

[17] A. Shirata, Y. Suto, C. Hikage, T. Shiromizu, and N. Yoshida, Phys. Rev. D **76**, 044026 (2007), arXiv:0705.1311.

[18] H. F. Stabenau and B. Jain, Phys. Rev. D **74**, 084007 (2006), arXiv:astro-ph/0604038.

[19] A. Knebe and B. K. Gibson, Mon. Not. R. Astron. Soc. **347**, 1055 (2004), arXiv:astro-ph/0303222.

[20] U. Seljak and M. Zaldarriaga, Astrophys. J. **469**, 437 (1996), arXiv:astro-ph/9603033.

[21] A. Klypin and J. Holtzman, ArXiv e-prints (1997), astro-ph/9712217.

[22] G. Efstathiou, M. Davis, S. D. M. White, and C. S. Frenk, Astrophys. J. Suppl. Ser. **57**, 241 (1985).

[23] A. Knebe, A. Green, and J. Binney, **325**, 845 (2001), arXiv:astro-ph/0103503.

[24] C. Power and A. Knebe, Mon. Not. R. Astron. Soc. **370**, 691 (2006), arXiv:astro-ph/0512281.

[25] J. S. Bagla and S. Ray, Mon. Not. R. Astron. Soc. **358**, 1076 (2005), arXiv:astro-ph/0410373.

[26] S. P. D. Gill, A. Knebe, and B. K. Gibson, Mon. Not. R. Astron. Soc. **351**, 399 (2004), arXiv:astro-ph/0404258.

[27] M. A. K. Gross, Ph.D. thesis, AA(UNIVERSITY OF CALIFORNIA, SANTA CRUZ) (1997).

[28] A. Knebe, A. V. Kravtsov, S. Gottlöber, and A. A. Klypin, Mon. Not. R. Astron. Soc. **317**, 630 (2000), arXiv:astro-ph/9912257.

[29] A. Klypin, S. Gottlöber, A. V. Kravtsov, and A. M. Khokhlov, Astrophys. J. **516**, 530 (1999), arXiv:astro-ph/9708191.

[30] M. Tegmark, D. J. Eisenstein, M. A. Strauss, D. H. Weinberg, M. R. Blanton, J. A. Frieman, M. Fukugita, J. E. Gunn, A. J. S. Hamilton, G. R. Knapp, et al., Phys. Rev. D **74**, 123507 (2006), arXiv:astro-ph/0608632.

[31] V. Springel, S. D. M. White, A. Jenkins, C. S. Frenk, N. Yoshida, L. Gao, J. Navarro, R. Thacker, D. Croton, J. Helly, et al., Nature (London) **435**, 629 (2005), arXiv:astro-ph/0504097.

[32] S. Gottlöber, E. L. Łokas, A. Klypin, and Y. Hoffman, Mon. Not. R. Astron. Soc. **344**, 715 (2003), arXiv:astro-ph/0305393.

[33] S. Kazantzidis, L. Mayer, C. Mastropietro, J. Diemand, J. Stadel, and B. Moore, Astrophys. J. **608**, 663 (2004), arXiv:astro-ph/0312194.

[34] A. V. Kravtsov, O. Y. Gnedin, and A. A. Klypin, Astrophys. J. **609**, 482 (2004), arXiv:astro-ph/0401088.

[35] K. L. Adelberger, C. C. Steidel, M. Pettini, A. E. Shapley, N. A. Reddy, and D. K. Erb, Astrophys. J. **619**, 697 (2005), arXiv:astro-ph/0410165.

[36] H. L. Morrison, P. Harding, K. Perrett, and D. Hurley-Keller, Astrophys. J. **603**, 87 (2004), arXiv:astro-ph/0307302.

[37] F. Hammer, M. Puech, L. Chemin, H. Flores, and M. D. Lehnert, Astrophys. J. **662**, 322 (2007), arXiv:astro-ph/0702585.

[38] A. Rawat, F. Hammer, A. K. Kembhavi, and H. Flores, Astrophys. J. **681**, 1089 (2008), arXiv:0804.0078.

[39] E. Zackrisson, N. Bergvall, T. Marquart, and G. Östlin, Astron. Astrophys. **452**, 857 (2006), arXiv:astro-ph/0603523.

[40] Random seed number is the same for each slice, so we compare particles with the same ID's in each simulation box.

[41] *Sloan Digital Sky Survey* http://www.sdss.org/